Electronic Supplementary Information

Deep-eutectic-solvent synthesis of N/O self-doped hollow carbon nanorods for efficient energy storage

Danfeng Xue,[a] Dazhang Zhu,[a] Hui Duan,[a] Zhiwei Wang,[b] Yaokang Lv,[c] Wei Xiong,[d] Liangchun Li,[a] Mingxian Liu,*[ab] Lihua Gan*[a]

[a]Shanghai Key Lab of Chemical Assessment and Sustainability, School of Chemical Science and Engineering, Tongji University, Shanghai 200092, P. R. China.

[b]State Key Laboratory of Pollution Control and Resources Reuse, Shanghai Institute of Pollution Control and Ecological Security, College of Environmental Science and Engineering, Tongji University, Shanghai 200092, P. R. China.

[c]College of Chemical Engineering, Zhejiang University of Technology, Hangzhou 310014, P. R. China.

[d]Key Laboratory for Green Chemical Process of Ministry of Education, School of Chemistry and Environmental Engineering, Wuhan Institute of Technology, 693 Xiongchu Road, Wuhan 430073, P. R. China.

*Corresponding Authors.

E-mail: liumx@tongji.edu.cn (M. Liu), ganlh@tongji.edu.cn (L. Gan)

Experimental section

Synthesis of HCNs

Urea (1 g) and 2,5-dihydroxy-1,4-benzoquinone (0.5 g) were dissolved in 10 mL distilled water at a ceramic crucible, and then various mass of $ZnCl_2$ (0−15 g) was added and stirred for formation of a uniform solution at room temperature. The solution was transferred to 105 °C oven and keep for 30 h for volatilization. Then the mixture was annealed in a tubular furnace under the N_2 flow with heating rate of 2.5 °C min^{-1} at target temperatures with a residence time of 1 h. After carbonization, the resulting samples were washed with dilute HCl solution twice for removal of Zn impurity. Subsequently, the HCNs were obtained after drying at 100 °C overnight. The obtained heteroatom-doped porous hollow carbon nanorods were designated as HCN-*x* where *x* represents the impregnation mass of $ZnCl_2$ (0, 1, 5, 10, 15 g). ZnO/HCN-10 is referred as HCN-10 without removal of ZnO.

Characterization

Thermo Nicolet NEXUS spectroscopy was employed to achieve Fourier-transform infrared (FT-IR) spectrum. The X-ray diffraction (XRD, Bruker D8) was utilized to analyze the amorphous structure of the samples. A Netzsch STA409 PC analyzer was employed to measure the ash content of the samples *via* thermogravimetric analysis (TGA) under air atmosphere at a heating rate of 10 °C min^{-1} from room temperature to 800 °C for 1 h. Inductively coupled plasma mass spectroscopy (ICP-MS) was measured on Optima 7300 DV to detect the concentration of zinc. The morphology and structure of the obtained samples was analyzed through transmission electron microscopy (TEM) and scanning electron microscopy (SEM), using a JEM-2100 electron microscope and a Hitachi S-4800 system, respectively. A micromeritics ASAP 2460 analyzer was

employed to study the porous texture of the carbons *via* the nitrogen sorption isotherms measured at −196 °C. The specific surface area of the sample was calculated by employing the Brumauer-Emmett-Teller (BET) method under P/P_0=0.05−0.25; The pore size distribution was calculated based on nonlocal density functional theory (NLDFT) equilibrium model method for slit pores. The surface functionality was analyzed using an AXIS Ultra DLD X-ray photoelectron spectroscope (XPS). Elemental analysis (EA) was performed on an Elementar vario EL cube elemental analyzer.

Electrochemical measurement

CHI660D electrochemical workstation was employed to investigate the electrochemical behaviors of obtained samples in 6 M KOH aqueous electrolyte for a three-electrode system configuration. The working electrode was assembled by a mixture of the prepared carbon sample ~3 mg, graphite (Shanghai Colloid Chemical Plant) and polytetrafluoroethylene (PTFE, catalog no. FR301B; Shanghai 3F New Materials Co., Ltd.) with a weight ratio of 8:1:1. The mixture was dispersed in ethanol to obtain a homogeneous slurry and followed dried at 100 °C overnight to obtain a dough, after that, rolled the resultant dough into a rounded working electrode (thickness: 0.25 mm; diameter: 0.5 cm, mass loading of electroactive materials: ~15 mg cm^{-2}) and pressed upon the current collector nickel foam (Shanghai Hongxiang Plant) under 20 MPa, and then was soaked in 6 M KOH electrolyte overnight. The counter and reference electrodes are nickel foam and saturated calomel electrode, respectively. The frequency range between 10^{-2} and 10^{6} Hz was set to measured electrochemical impedance spectroscopy (EIS) of electrode materials. Galvanostatic charged-discharged (GCD) and cyclic voltammetry (CV) were tested at a voltage between −1.0 and 0 V. The gravimetric capacitance of single electrode was calculated *via* following equation:

$$C_m = \frac{I \times \Delta t}{m \times \Delta V} \quad (1)$$

C_m: (F g^{-1}): gravimetric specific capacitance (F g^{-1}); I (A): discharge current; Δt (s): discharge time; m (g): electroactive materials of single electrode; ΔV (V): operation voltage (−1.0 − 0).

In symmetric supercapacitors, CV and GCD were tested in 6 M KOH, 1 M Na_2SO_4, 7 m (mol-salt in kg-solvent) lithium bis(trifluoromethane sulfonyl)imide (LiTFSI) solution, and ionic liquid 1-ethyl-3-methylimidazolium tetrafluoroborate ($EMIMBF_4$) electrolyte, respectively. The composition of the working electrode for two-electrode cell is the same as that of three-electrode system. Two identical working electrodes (circular shape, diameter: 8 mm, active material: ~5 mg) were pressed onto two current collectors (stainless-steel mesh, circular shape, diameter: 14 mm) at 20 MPa, respectively. The working electrodes were packed in a 2016-type coin cell together with a polypropylene membrane separator (Celgard 3501, 11 Technology Co., Ltd.) and above-mentioned electrolyte (80 μL). The gravimetric capacitance (C_m), energy density (E) and power density (P) were calculated as follow:

$$C_m = 4C_{cell} = \frac{4I \times \Delta t}{m_{\text{two}} \times \Delta V} \quad (2)$$

$$E = \frac{C_{cell} V^2}{7.2} \quad (3)$$

$$P = \frac{E}{\Delta t} \quad (4)$$

C_{cell}: (F g^{-1}): gravimetric specific capacitance of the cell (F g^{-1}); I (A): discharge current; Δt (s): discharge time; m_{two} (g): the total mass of active substance in two electrodes; ΔV (V): operation voltage.

For a comparison, the two-electrode cell using the reference activated carbons (ACs, FCO-20A; Zhejiang Forasen Energy Technology Co., China) with a surface area of 1880 m^2 g^{-1} as electrode materials was assembled and measured by using the same manner as that for the HCNs.

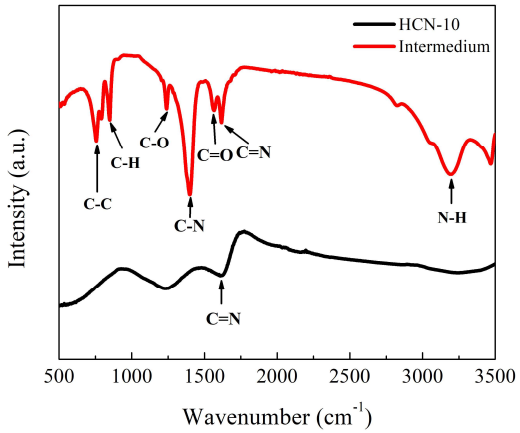

Figure S1. FT-IR spectra of intermedium and HCN-10.

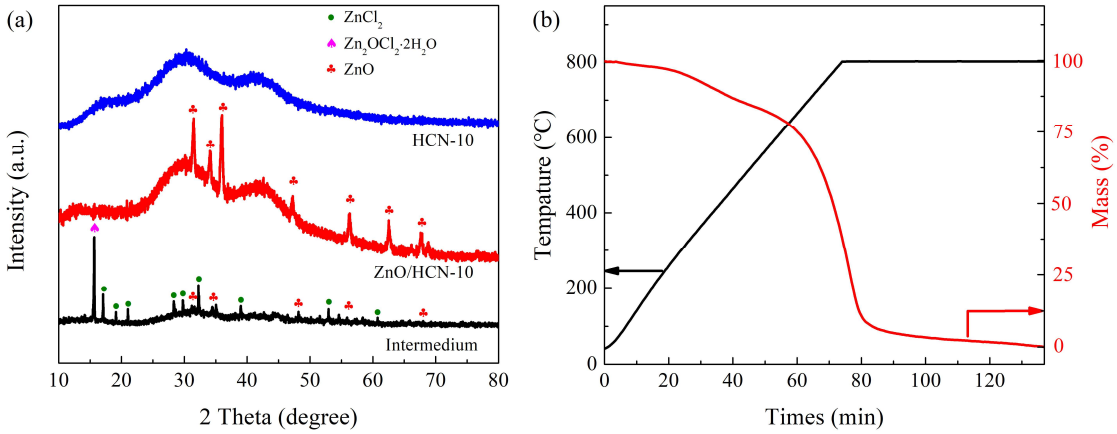

Figure S2. XRD patterns of intermediate, ZnO/HCN-10 and HCN-10 (a); TGA curve of HCN-10 (b).

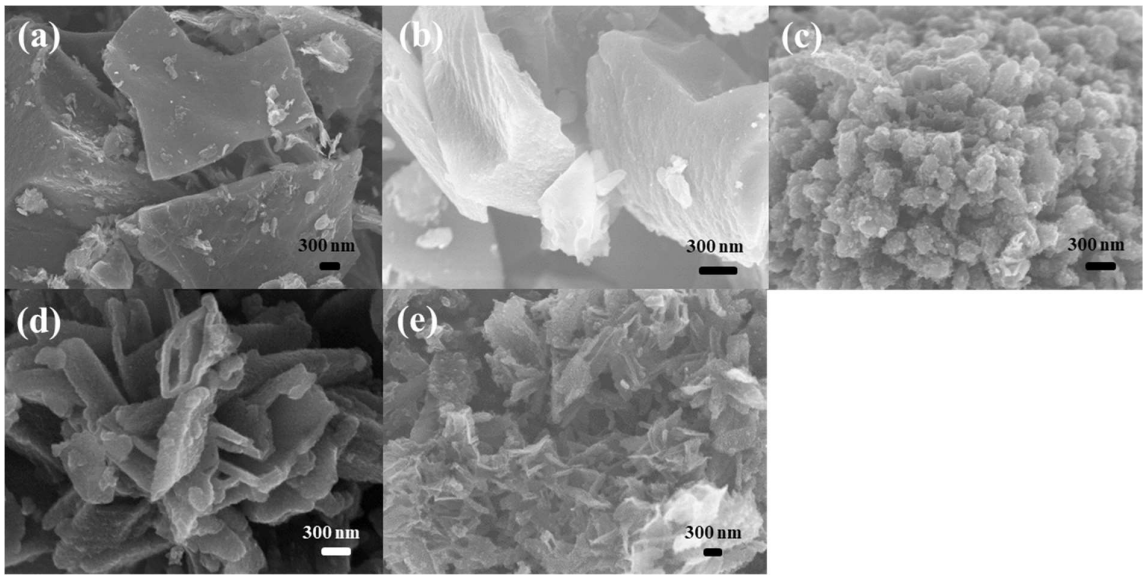

Figure S3. SEM images of HCN-0 (a), HCN-1 (b), HCN-5 (c), HCN-10 (d) and HCN-15 (e).

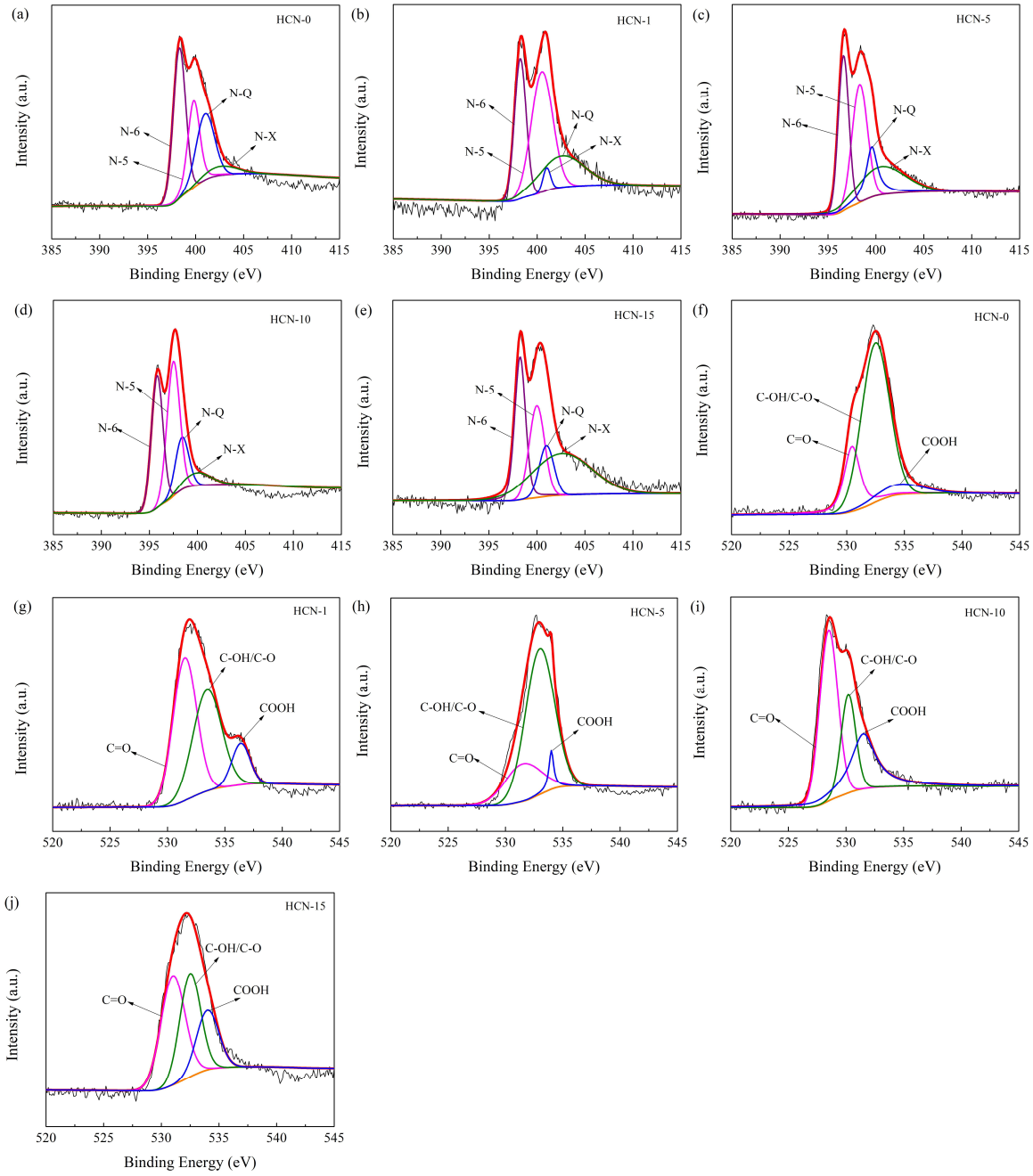

Figure S4. N 1s (a–e) and O 1s (f–j) high-resolution spectra of HCNs.

Table S1. Summary of XPS analysis of HCNs.

Samples	N (wt%)	O (wt%)	The relative intensity of the dopant species (%)				
			N-6	N-5	N-Q	N-X	N-5+N-6
HCN-0	18.4	12.4	32.2	23.9	28.3	15.6	56.2
HCN-1	13.9	8.5	25.8	30.9	11.0	32.3	56.7
HCN-5	11.1	8.4	28.7	29.4	15.4	26.5	58.1
HCN-10	8.1	10.1	32.3	36.9	15.4	15.2	69.4
HCN-15	7.7	8.1	25.3	20.9	13.6	40.2	46.2

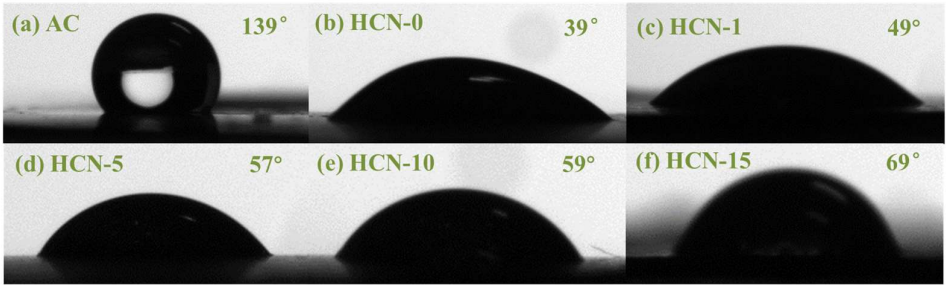

Figure S5. Wetting angles of water droplet on activated carbons (AC, a) and HCNs (b−f).

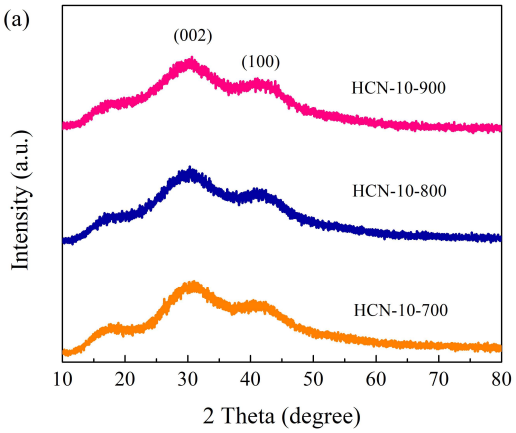

Figure S6. XRD patterns of HCN-10-*T*.

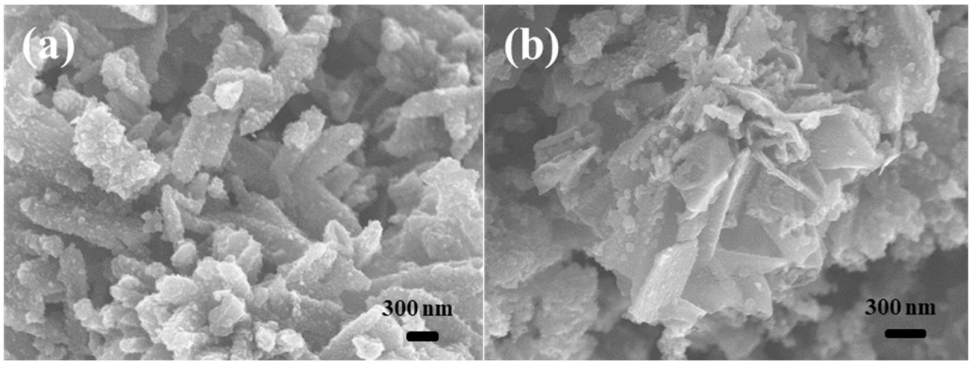

Figure S7. SEM images of HCN-10-700 (a) and HCN-10-900 (b).

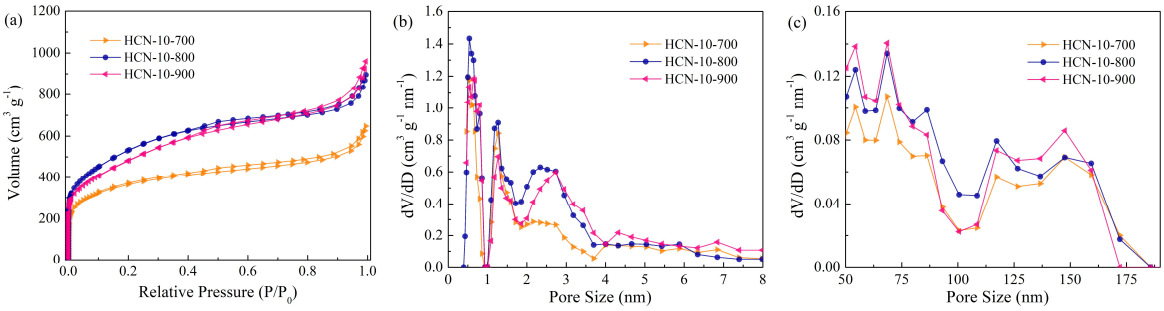

Figure S8. Nitrogen sorption isotherms (a) and the curves of pore size distribution (b and c) of HCN-10-*T*.

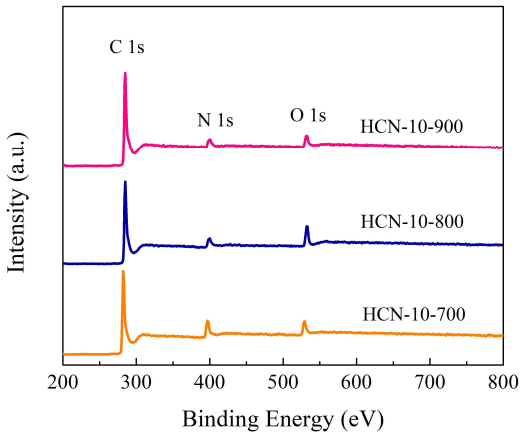

Figure S9. Wide-scan XPS spectra of HCN-10-*T*.

Table S2. The porosity parameters, bulk and surface element contents and contact angles of HCN-10-*T*.

Samples	S_{BET} (m^2 g^{-1})	S_{micro} (m^2 g^{-1})	EA		XPS		Contact angles (°)
			N (wt%)	O (wt%)	N (wt%)	O (wt%)	
HCN-10-700	1224	989	12.4	11.1	12.8	12.0	45
HCN-10-900	1513	1053	5.4	8.2	5.33	8.3	72

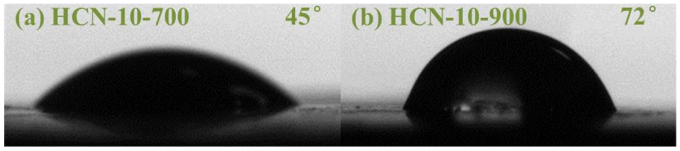

Figure S10. Wetting angles of water droplet on HCN-10-700 (a) and HCN-10-900 (b).

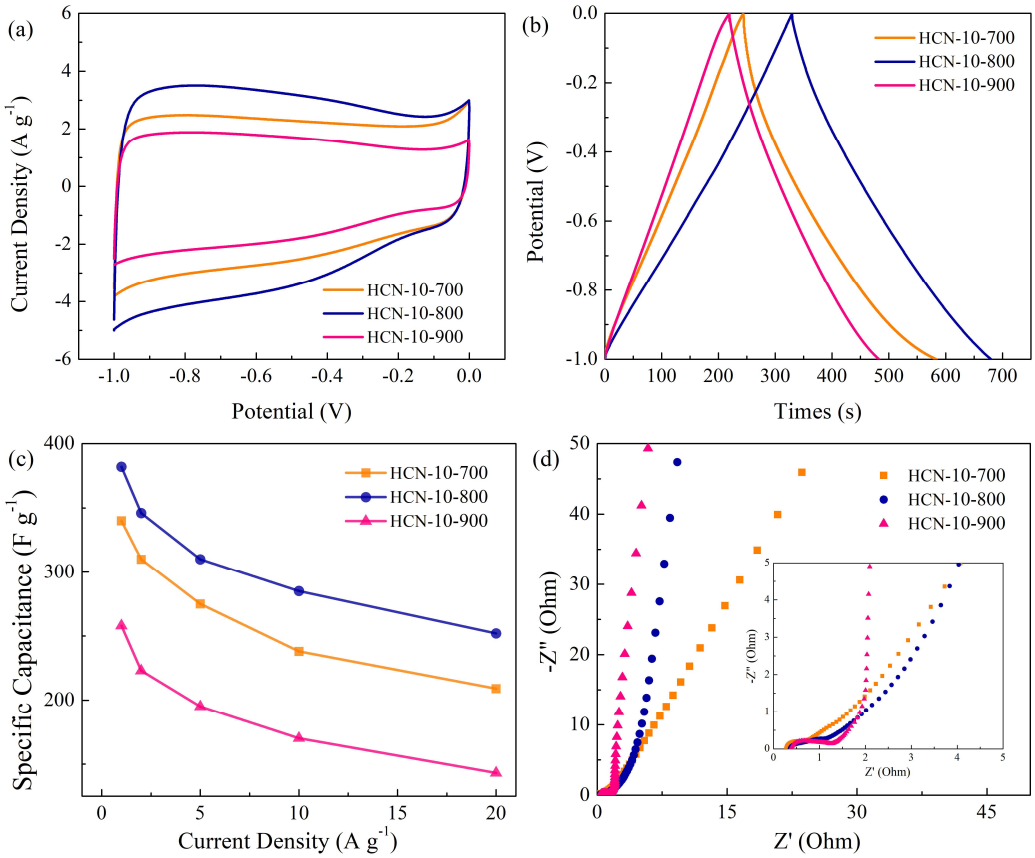

Figure S11. Electrochemical performances of HCN-10-*T* electrodes measured in a three-electrode system using 6 M KOH electrolyte: CV curves at 20 mV s^{-1} (a), GCD curves at 1.0 A g^{-1} (b), rate performancs (c), and Nyquist plots (d).

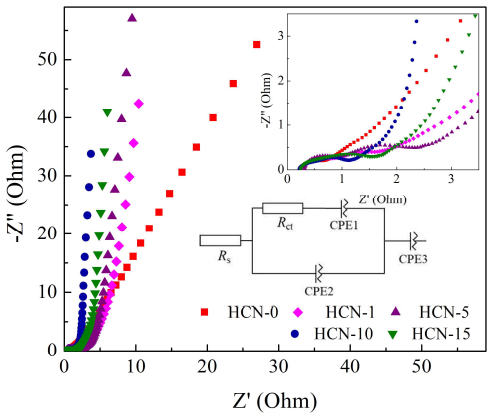

Figure S12. Nyquist plots and the equivalent circuit model of HCN electrodes in 6 M KOH electrolyte.

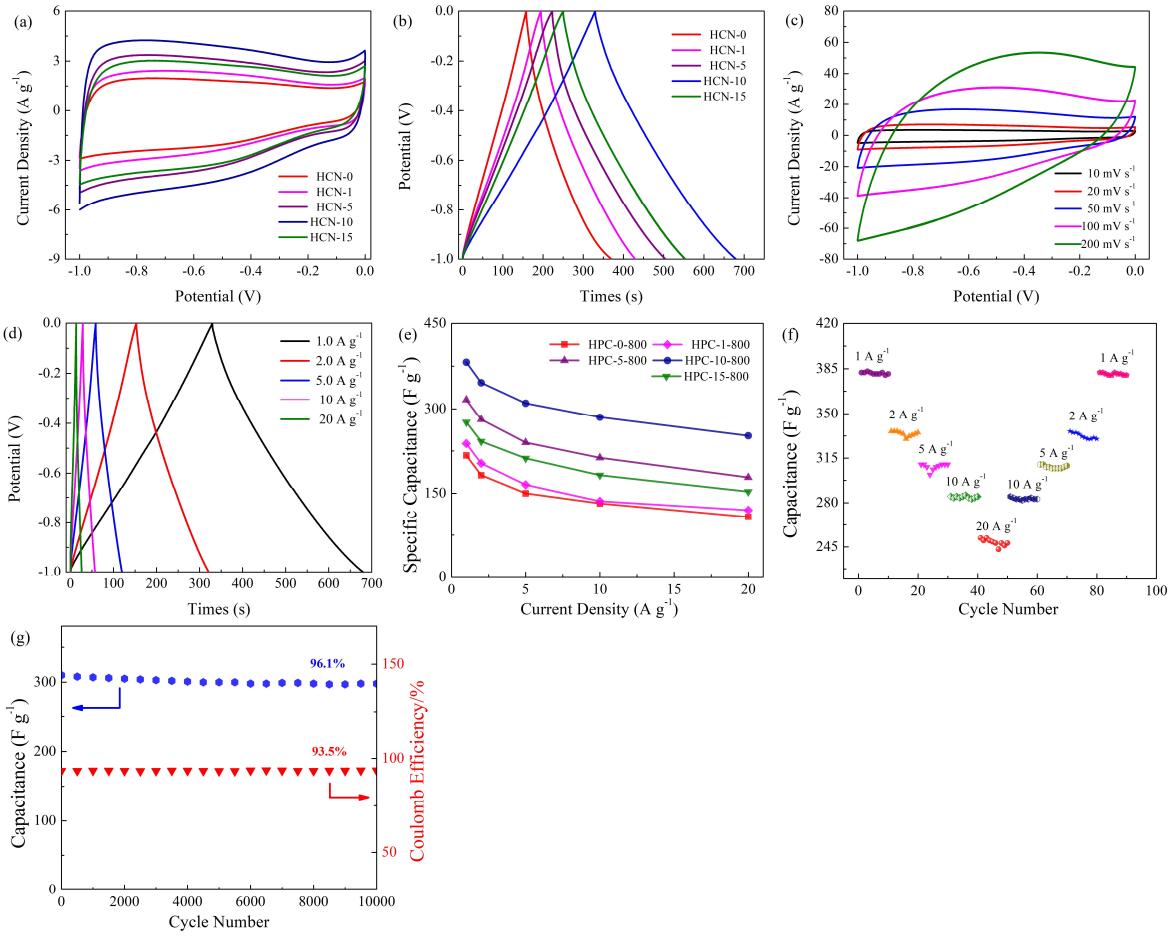

Figure S13. Electrochemical performances of HCN electrodes measured in a three-electrode system using 6 M KOH electrolyte: CV curves at a scan rate of 20 mV s^{-1} (a); discharge–charge curves at 1.0 A g^{-1} (b); CV curves of HCN-10 electrode at various scan rates (c); GCD curves of HCN-10 electrode at various current densities (d); capacitances *vs*. current densities of HCN electrodes (e); rate capability (f) and cycle performance and Coulombic efficiency (g) of HCN-10 electrode.

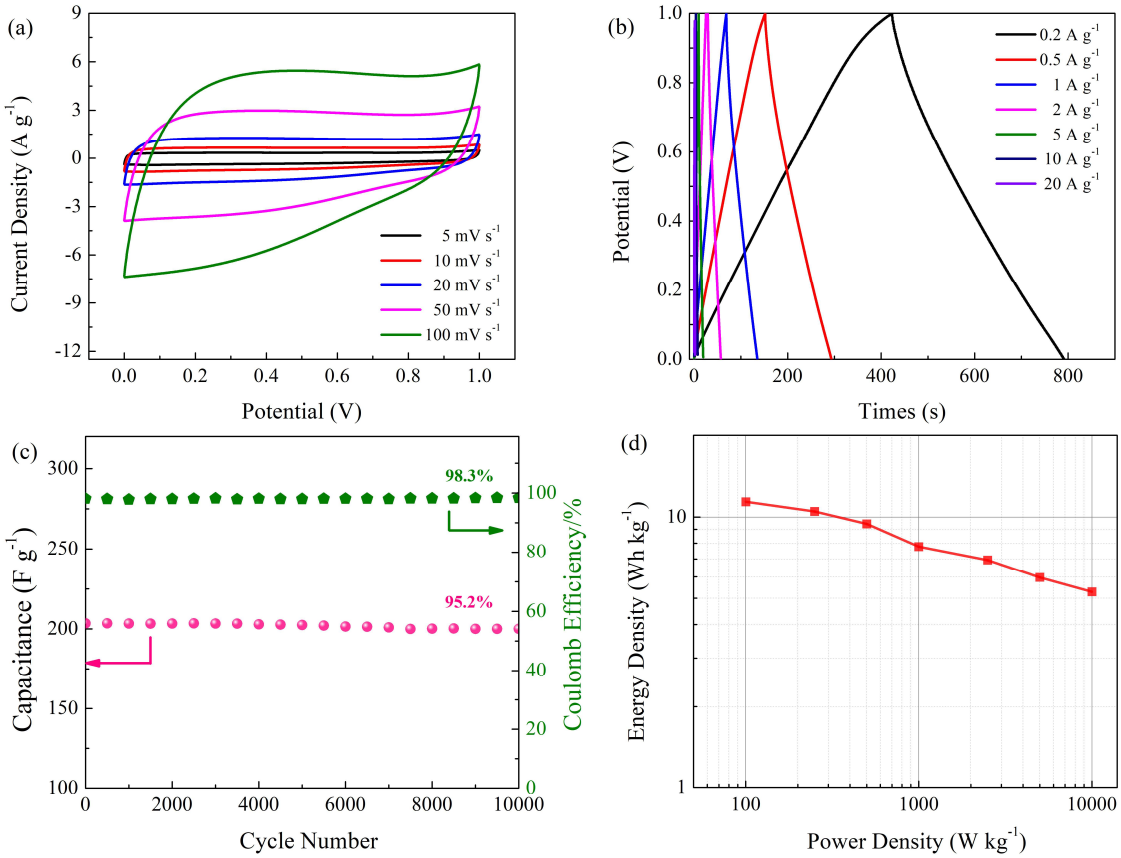

Figure S14. Electrochemical performances of HCN-10 electrode measured in a two-electrode system using 6 M KOH electrolyte: CV curves at various scan rates (a), GCD curves at different current densities (b), cycling stability and Coulombic efficiencies at 5.0 A g^{-1} over 10,000 cycles (c), and Ragone plots (d).

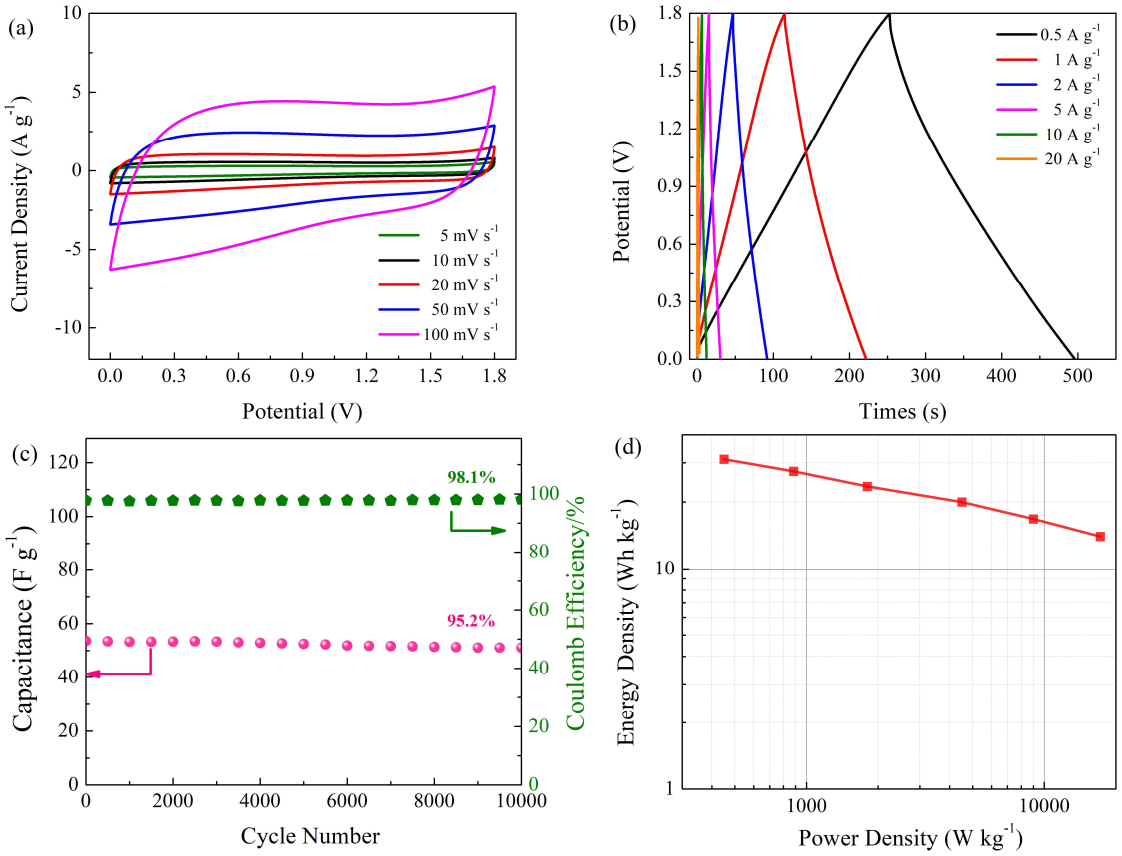

Figure S15. Electrochemical performances of HCN-10 based symmetric supercapacitor employing Na_2SO_4 electrolyte: CV curves at different scan rates (a), GCD curves at various current densities (b), cycling stability and Coulombic efficiencies at 2.0 A g^{-1} over 10,000 cycles (c), and Ragone plots (d).

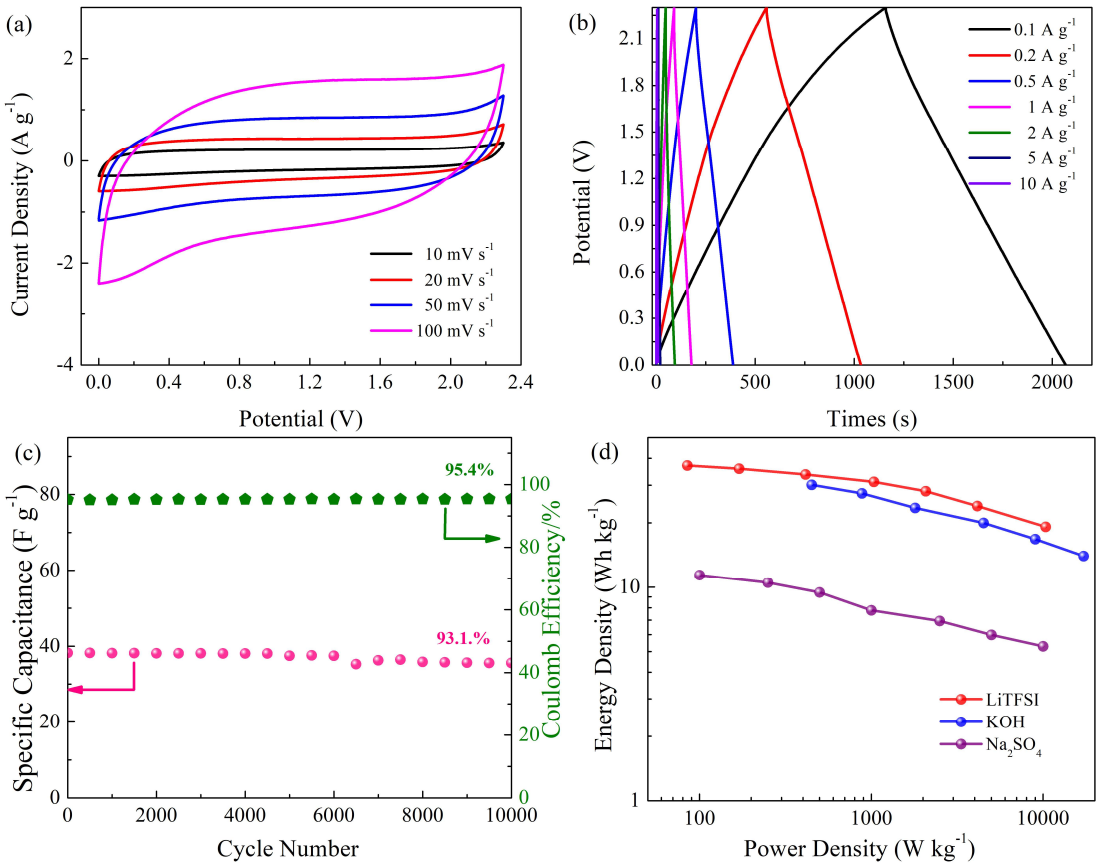

Figure S16. Electrochemical behaviors of HCN-10 based symmetric supercapacitor using 7 m LiTFSI electrolyte: CV curves at different scan rates (a), GCD curves at various current densities (b), cycling stability and Coulombic efficiencies at 2.0 A g^{-1} over 10,000 cycles (c) and Ragone plots (d).

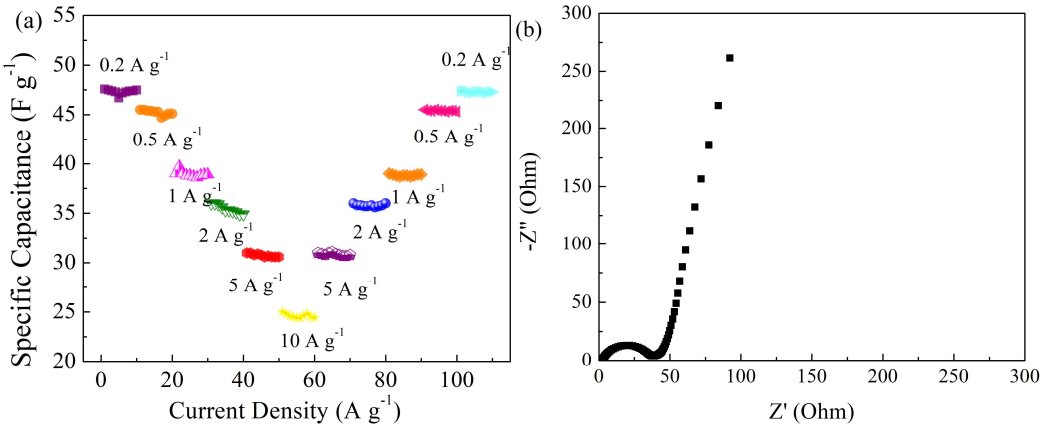

Figure S17. Rate performances (a) and Nyquist plots (b) of HCN-10 based symmetric supercapacitor using an $EMIMBF_4$ electrolyte.

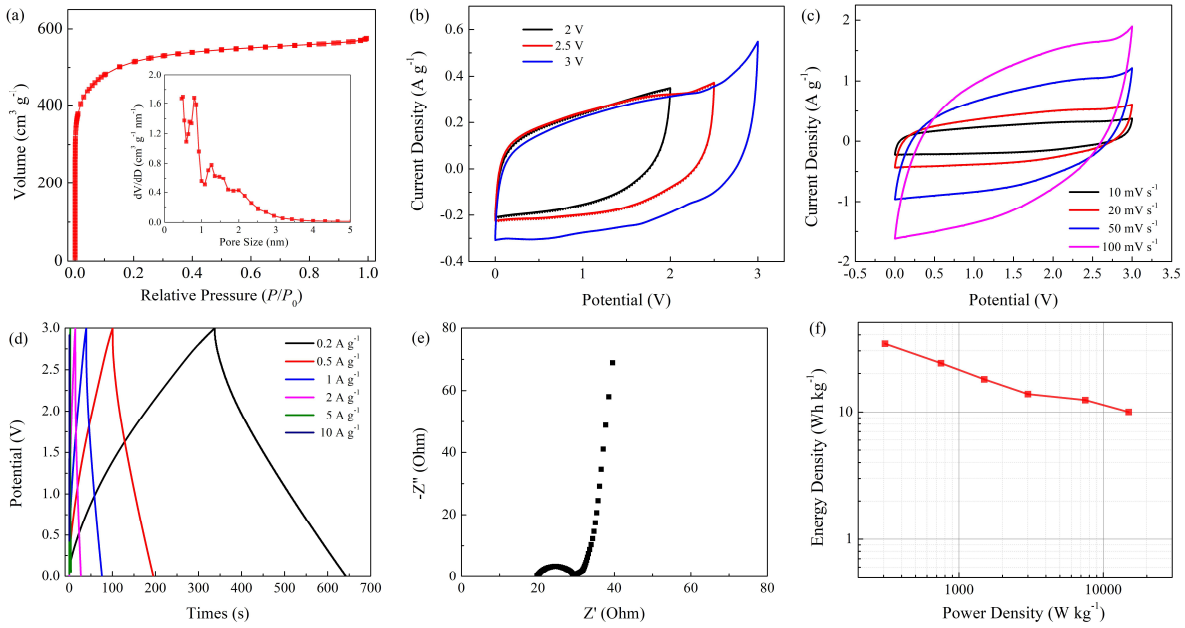

Figure S18. Nitrogen sorption isotherm and the curve of pore size distribution of ACs (a). Electrochemical behaviors of commercial ACs based symmetric supercapacitor using $EMIMBF_4$ electrolyte: CV curves at various voltage window under 10 mV s^{-1} (b); CV curves at different scan rates (c), GCD curves at various current densities (d), Nyquist plots (e) and Ragone plots (f).